Composition–electric field phase diagram of the Pb-free piezoelectric system $Na_{0.5}Bi_{0.5}TiO_3$-$BaTiO_3$

Gobinda Das Adhikary,* Gudeta Jafo Muleta, and Rajeev Ranjan†
Department of Materials Engineering, Indian Institute of Science, Bangalore 560012, India

(Received 22 October 2023; revised 14 November 2023; accepted 21 November 2023; published 7 December 2023)

$(1-x)Na_{0.5}Bi_{0.5}TiO_3$-$(x)BaTiO_3$ is one of the important Pb-free piezoelectric alloy systems. Despite extensive investigation over the years, the composition x–electric field (E) phase diagram of this alloy system has not received sufficient attention. Here, we performed an x-ray diffraction study *in situ* with electric fields at close composition intervals in a wide range: $0.0 \leqslant x \leqslant 0.18$. We discovered that this system exhibits field-driven, reversible interferroelectric transformations in a large composition range: $0.02 < x < 0.14$. Based on this work, we present the first comprehensive x-E phase diagram of this system. Apart from addressing inconsistencies in an earlier study, our phase diagram can precisely explain the composition trend of both the weak-field (dielectric and piezoelectric) and high-field (electrostrain) properties of this Pb-free piezoelectric system.

DOI: 10.1103/PhysRevB.108.224105

Many critical engineering applications of functional materials are derived from the extraordinary responses of inherent or emergent properties at phase instabilities. Examples include large piezoelectricity in ferroelectric alloys [1–4], large magnetostriction in rare earth-based ferromagnets [5], colossal magnetoresistance in manganites [6], etc. Advanced piezoelectrics are sought after as compact and energy-efficient actuators and transducers [7]. They are ferroelectric alloys with compositions close to a morphotropic phase boundary (MPB) representing an interferroelectric instability in the composition (x)-temperature (T) phase diagram [8]. For over six decades, MPB compositions of $Pb(Zr_xTi_{1-x})O_3$-based piezoelectrics have been used in wide-ranging applications. However, legislation restricting hazardous substances in electronic devices [9] has increased attention to nontoxic, Pb-free piezoelectrics [10–12]. MPB solid solutions of the Pb-free ferroelectrics like $BaTiO_3$ [3,13–17], $KNbO_3$ [18,19], $BiFeO_3$ [20], $Na_{0.5}Bi_{0.5}TiO_3$ (NBT) [21–25], and $K_{0.5}Bi_{0.5}TiO_3$ [26] have received significant attention in this regard. Among them, the NBT-based piezoelectrics have attracted particular attention for their ability to exhibit relatively higher levels of electrostrain (>0.5%) in comparison to $Pb(Zr,\ Ti)O_3$ [27–30].

Although the MPB compositions are attractive for their large weak-field electromechanical (piezoelectric) response, hysteresis becomes a major concern in applications involving high-field cyclic processes. The MPB compositions exhibiting a maximum electromechanical response also show large hysteresis, which is detrimental from the application perspective. A careful balance between enhanced electromechanical response and low hysteresis requires a detailed understanding of the phase diagrams, not only as a function of composition (x) and temperature (T) but also as a function of composition (x) and electric field (E). While the composition (x)-temperature (T) phase diagram of NBT-$BaTiO_3$ has significantly evolved over the years [24,31–33], the x-E phase diagram has not received sufficient attention. A good understanding of the high-field properties has yet to be developed for this Pb-free piezoelectric system. The previously reported x-E phase diagram was solely based on transmission electron microscopy (TEM) examination *in situ* with a field of three representative compositions ($x = 0.055$, 0.06, and 0.07) in close proximity to the MPB ($x = 0.06$) [24,34]. Except for a very limited composition range ($0.05 < x < 0.07$), the depiction of the phases in this phase diagram [24,34] is not consistent with the conclusions of several x-ray diffraction studies (XRD) [33,35–37]. For example, while the XRD studies suggest tetragonal ($P4mm$) ferroelectric distortion for the unpoled non-MPB compositions $x > 0.07$, this compositional range is instead depicted as the $P4bm$ relaxor phase, which irreversibly transforms to the ferroelectric tetragonal ($P4mm$) phase only at high fields ($\sim 20\,kV/cm$). Such inconsistencies can be a source of confusion concerning our understanding of the properties. The plausibility of an x-E phase diagram should also be tested on its ability to explain the weak-field and high-field properties trend across compositions. With this motivation, we investigated the E-driven structural transformation behavior and high-field/weak-field property measurements over the entire composition range of interest ($0 \leqslant x \leqslant 0.18$). We discovered new E-driven phase transition scenarios and metastable regimes. Our x-E phase diagram explains both the weak-field (dielectric constant, piezoelectric coefficient) and high-field (ferroelectric polarization, electrostrain) property trends with all its subtle details.

$(1-x)Na_{0.5}Bi_{0.5}TiO_3$-$(x)BaTiO_3$ (NBT-xBT) [$(0.00 \leqslant x \leqslant 0.18)$] specimens were synthesized using the conventional solid-state reaction method, the details of which can be found in the Supplemental Material Appendix S1 [38]. We performed an XRD study *in situ* with a unipolar electric field applied on virgin (unpoled) pellets. Experiments were carried out at close composition intervals in the

*Corresponding author: gadhikary53@gmail.com
†Corresponding author: rajeev@iisc.ac.in

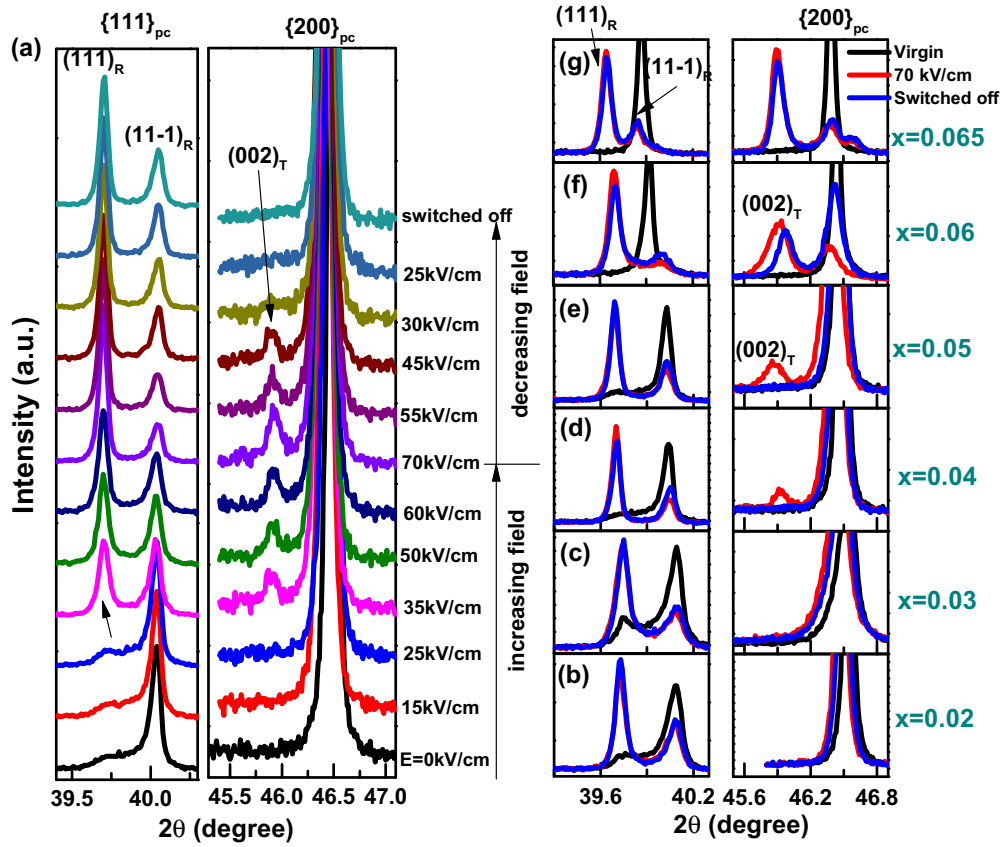

FIG. 1. (a) Evolution of the XRD Bragg profiles of $\{111\}_{pc}$ and $\{200\}_{pc}$ pseudocubic reflections as a function of increasing and decreasing field for $x = 0.04$ of NBT-(x)BT. An additional peak appears just before the $\{200\}_{pc}$ peak at 35 kV/cm This additional peak corresponds to the $(002)_T$ peak of the tetragonal $P4mm$ phase. (b)–(g) show the $\{111\}_{pc}$ and $\{200\}_{pc}$ XRD Bragg profiles of (b) $x = 0.02$, (c) $x = 0.03$, (d) $x = 0.04$, (e) $x = 0.05$, (f) $x = 0.06$, and (g) $x = 0.065$ in the virgin state (black), at 70 kV/cm (red), and after switching off the field (blue). It is important to note that the tetragonal peak appears when the field is on and disappears after switching off the field.

range of $0.00 \leqslant x \leqslant 0.18$. Consistent with a previous study [39], NBT ($x = 0$) exhibits $Cc \rightarrow R3c$ irreversible transformation with increasing field (Supplemental Material Fig. S1 [38]). All $x < 0.03$ show a similar transformation behavior (Supplemental Material Fig. S2(a) [38]). Additional features can be seen for $0.03 \leqslant x < 0.06$, which exhibit a rhombohedral ($R3c$) structure (Figs. 1(c)–1(e) and Supplemental Material Fig. S2(b) [38]) even in the unpoled state [22,24]. For example, in addition to the common phenomenon of field-induced preferred orientation due to switching of the rhombohedral domains, an additional peak at $2\theta \sim 45.91^\circ$ [just before the $(200)_R$ peak] appears at $E \sim 35\,\mathrm{kV/cm}$ for $x = 0.04$. As discussed later, this additional peak's position matches the $(002)_T$ position of the tetragonal ($P4mm$) ferroelectric phase. Thus, unlike for $x < 0.03$, $x = 0.04$ exhibits a field-induced $R3c \rightarrow P4mm$ transformation. We limited the maximum electric field to 70 kV/cm as a higher field increased the chances of dielectric breakdown. On reducing the field strength, the tetragonal phase vanished below $\sim 27\,\mathrm{kV/cm}$ [Fig. 1(a)]. This confirms the reversible nature of the E-driven $R3c$-$P4mm$ transformation. All compositions in the range $0.03 \leqslant x < 0.06$ show the same transformation behavior [Fig. 1(e) and Supplemental Material Fig. S2(b) [38]). No such phase transformation scenario has been depicted in the available x-E phase diagram [34].

The next crossover happens at $x = 0.06$, the MPB composition that appears as a cubic-like phase (CL) on a global scale [22,33,36,40]. At 10 kV/cm, the split of both $\{111\}_{pc}$ and $\{200\}_{pc}$ pseudocubic profiles confirms CL $\rightarrow$ rhombohedral ($R3c$) + tetragonal ($P4mm$) transformation (Supplemental Material Fig. S2(c) [38]). The field-induced coexistence of $R3c$ and $P4mm$ persists even after the removal of the field, confirming the irreversible nature of this transformation. The two other neighboring compositions, $x = 0.065$ (Supplemental Material Fig. S2(d) [38]) and $x = 0.07$ (Supplemental Material Fig. S3(a) [38]), show similar behavior. Our observations are at variance with previous studies [24,34,35], which indicate that at a field of $\sim 70\,\mathrm{kV/cm}$, $x = 0.06$ and $x = 0.07$ should exhibit $R3c$ and $P4mm$ phases, respectively. The absence of the rhombohedral phase in unpoled $x \geqslant 0.08$ marks another crossover. These compositions show only the $P4mm$ tetragonal distortions on a global scale [Figs. 2(c)–2(g)]. For $x = 0.08$, in addition to the E-driven preferred orientation of the tetragonal domains, which can be seen to have started at 8 kV/cm, the $\{111\}_{pc}$ pseudocubic Bragg profile develops a shoulder at 24 kV/cm. The $\{111\}_{pc}$ split is a signature of the rhombohedral ($R3c$) phase [Fig. 2(a)]. That this $P4mm \rightarrow$

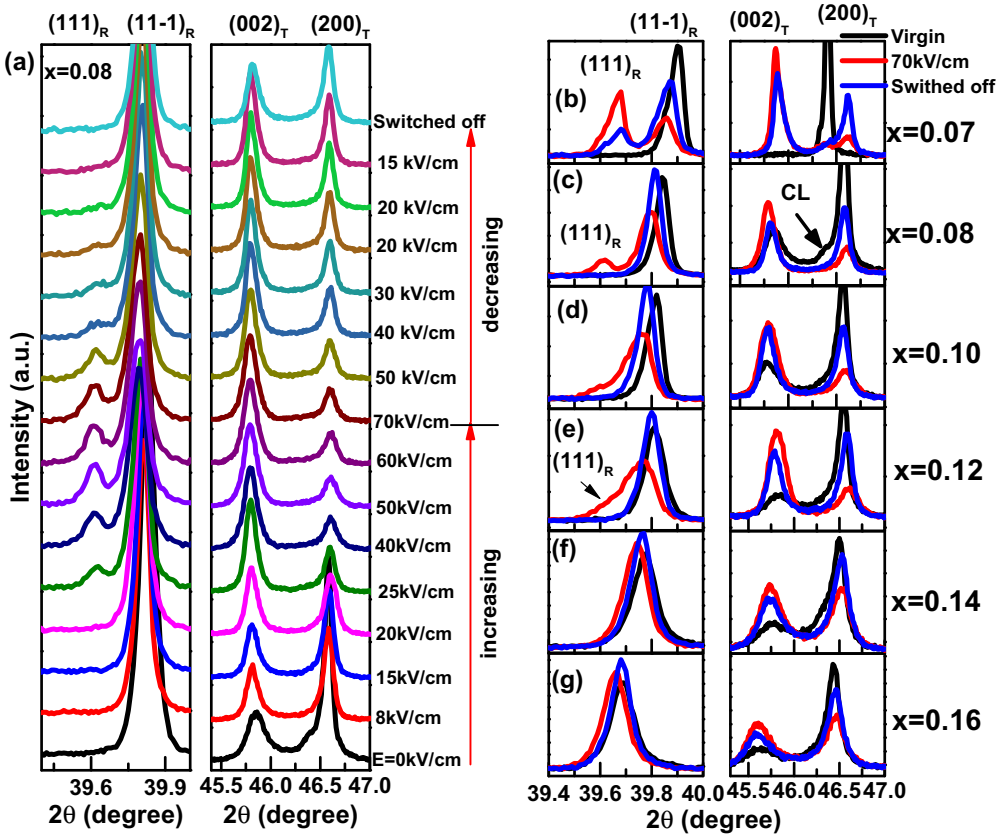

FIG. 2. (a) Evolution of $\{111\}_{pc}$ and $\{200\}_{pc}$ pseudocubic Bragg profiles as a function of increasing and decreasing field for $x = 0.08$. The $\{111\}_{pc}$ splits into two above 20 kV/cm, suggesting the onset of the *R*3*c* phase. This phase disappears at 20 kV/cm during the decreasing cycle. (b)–(g) show the $\{111\}_{pc}$ and $\{200\}_{pc}$ x-ray Bragg profiles of (b) $x = 0.07$, (c) $x = 0.08$, (d) $x = 0.10$, (e) $x = 0.12$, (f) $x = 0.14$, and (g) $x = 0.16$ in the virgin state (black), at 70 kV/cm (red), and after switching off the field (blue).

*R*3*c* transformation is reversible is evident from the disappearance of the rhombohedral peak when the field strength is reduced to 15 kV/cm. The compositions $0.08 < x \leqslant 0.12$ show the same E-driven transformation behavior [Figs. 2(d) and 2(e)]. For $x > 0.12$, the propensity for the rhombohedral distortion ceases (Figs. 2(f) and 2(g), and Supplemental Material Figs. S3(c) and S3(d) [38]).

We used these observations to draw a comprehensive *x*-E phase diagram of NBT-(*x*)BT (Fig. 3). For the sake of clarity concerning the reversible and irreversible evolution of the phases, the phase diagram is shown both as a function of increasing and decreasing field on the vertical axis. The most remarkable feature of this phase diagram is the coexistence of the *P*4*mm* and *R*3*c* phases in a wide composition range of $0.03 \leqslant x \leqslant 0.12$ above 40 kV/cm. That the tetragonal *P*4*mm* phase could be induced with an electric field in $0.03 \leqslant x < 0.06$, but not in $x < 0.03$ implies that the *P*4*mm* phase is metastable in the zero field state of $0.03 \leqslant x < 0.06$, but not for $x < 0.03$. Similarly, the ability of the electric field to induce the rhombohedral phase in $0.08 \leqslant x \leqslant 0.12$, but not for $x > 0.12$ indicates that the rhombohedral phase is metastable in the zero field state for $0.07 \leqslant x \leqslant 0.12$ but not so for $x > 0.12$. The MPB composition range $0.06 \leqslant x \leqslant 0.07$, on the other hand, represents the stability of both the ferroelectric phases in the zero field state.

It is worth highlighting the qualitative differences in our *x*-E diagram (Fig. 3) and the one available in the literature [24,34]. First, the previous *x*-E diagram depicted the E-induced transformations to be irreversible for all compositions $0.06 \leqslant x \leqslant 0.10$, whereas our findings limit the irreversibility only for $0.06 \leqslant x \leqslant 0.07$. Second, our findings do not support the relaxor *P*4*bm*-ferroelectric *P*4*mm* phase boundary depicted earlier at $E \sim 25\,\mathrm{kV/cm}$ for $x > 0.07$ in Refs. [24] and [34]. Given that the *P*4*bm* tetragonal phase is ferrielectric (weak polarization) and the *P*4*mm* tetragonal phase is ferroelectric (relatively strong polarization), a *P*4*bm*-to-*P*4*mm* transformation is expected to show an abrupt increase in the tetragonality above 25 kV/cm. As shown in Supplemental Material Fig. S4 [38], no such feature can be seen. We argue that the local in-phase octahedral tilt (characterized as the *P*4*bm* distortion) and their evolution with the electric field, picked up in TEM studies [34], may not qualify them as a thermodynamic phase to represent in the phase diagram. In this context, similar local *P*4*bm* regions are also seen in the TEM study of unpoled NBT [21]. However, this local distortion is not depicted as a phase in any of the reported *x*-*T*/*x*-E phase diagrams [24,34,41–43]. The *P*4*bm*-*P*4*mm* boundary depicted at $x \sim 0.12$ in the *x*-E phase diagrams of Refs. [24] and [34] can be referred to as a pseudoboundary separating two similar tetragonal *P*4*mm* (I)-*P*4*mm* (II) phases.

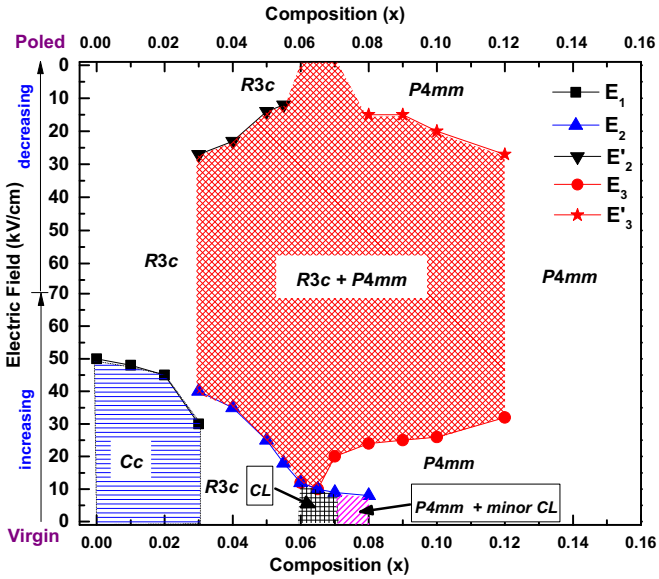

FIG. 3. Composition–electric field phase diagram of NBT-(x)BT. E_1, fields at which the monoclinic (Cc) to rhombohedral ($R3c$) transition occurs for $0.00 \leqslant x \leqslant 0.03$. E_2 and E_3, fields corresponding to the onset of the tetragonal ($P4mm$) phase and the onset of the $R3c$ phase, respectively; $E_2^{'}$ and $E_3^{'}$ pertains to the disappearance of the tetragonal ($P4mm$) phase and the disappearance of the $R3c$ phase when the field is reduced (for $0.03 \leqslant x \leqslant 0.12$). The red shaded region highlights $R3c + P4mm$ phase coexistence in an extended range ($0.03 \leqslant x \leqslant 0.12$).

The qualitative difference is that $P4mm$ (I) shows a $P4mm \rightarrow R3c$ transformation, but not by the $P4mm$ (II) phase.

We examined the implications of our observations on the high-field, cyclic unipolar electrostrain behavior [Figs. 4(a) and 4(b)] across the entire composition range. The strain (S) is maximum for $x = 0.08$, the single-phase tetragonal $P4mm$ composition just at the boundary of the $R3c + P4mm$ MPB region. The strain decreases continuously on either side of this composition and almost saturates for $x < 0.03$ and $x > 0.12$ [Fig. 4(c)]. We also estimated the composition dependence of the degree of S-E hysteresis, defined as ΔS (%), $= S_1(\%)$-$S_2(\%)$, at $E_{max}/2$ (see Supplemental Material Fig. S5 [38] for details). It follows the same trend with composition as the strain [Fig. 4(d)]. The strain hysteresis and the magnitude of the strain become almost composition independent for $x < 0.03$ and $x > 0.12$. This is consistent with the fact that the x-E phase diagram (Fig. 3) shows no field-driven interferroelectric transformation for these compositions. We also found that the two weak-field properties, longitudinal direct piezoelectric coefficient (d_{33}) and relative permittivity, follow the same trend as the high-field properties [Fig. 4(e) and 4(f)]. Though these properties do not correlate directly with the field-induced transformations depicted in Fig. 3, they indicate the compositional regime, which has polar heterogeneity because of the metastable phases. The near-composition independence of the weak-field properties for $x < 0.03$ and $x > 0.12$ manifests the absence of metastable phases.

In summary, based on the x-ray diffraction study *in situ* with an electric field study of $(1-x)Na_{0.5}Bi_{0.5}TiO_3$-$(x)BaTiO_3$ over a large compositional space, we present the first comprehensive x-E phase diagram of this Pb-free piezoelectric system. We show that (i) the pre-MPB compositions $0.03 \leqslant x \leqslant 0.05$ exhibit field-induced reversible rhombohedral ($R3c$) to tetragonal ($P4mm$) transformation, and (ii) the post-MPB compositions $0.07 < x < 0.14$ exhibit field-induced reversible tetragonal ($P4mm$) to rhombohedral transformation. We establish a one-to-one correspondence between this transformation behavior and the composition trend of electrostrain and hysteresis. Our phase diagram can also precisely explain the composition trend of the piezoelectric charge coefficient of this system. In the process, we resolve some inconsistencies in the previous understanding of the x-E diagram of this system.

G.D.A. and R.R. acknowledge the Science and Engineering Research Board for financial assistance (Grant No. CRG/2021/000134).

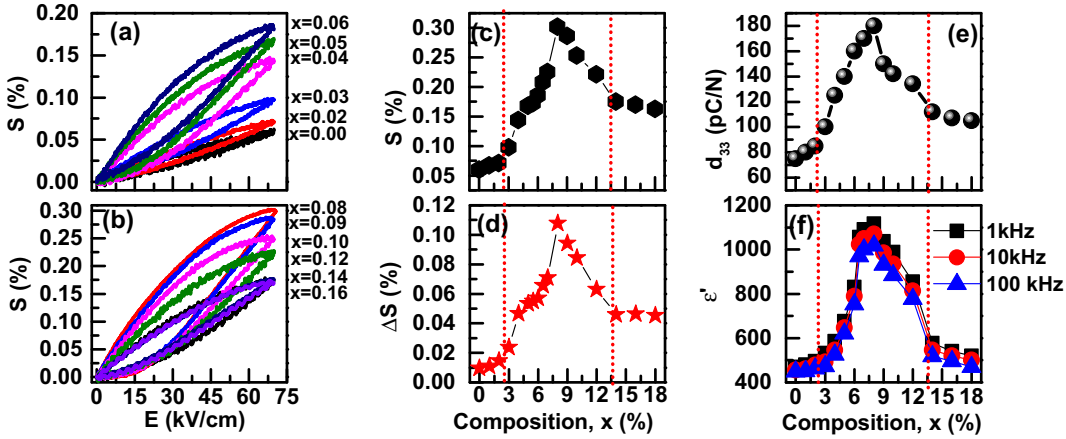

FIG. 4. (a), (b) Electric field-dependent unipolar strain for different compositions of (1-x)NBT-(x)BT. Composition dependence of (c) electrostrain S (%), (d) strain hysteresis ΔS (%) under unipolar cycling, (e) longitudinal piezoelectric coefficient d_{33}, and (f) dielectric constant ε' of poled specimens at frequencies of 1 kHz, 10 kHz, and 100 kHz.

[1] F. Li, D. Lin, Z. Chen, Z. Cheng, J. Wang, C. Li, Z. Xu, Q. Huang, X. Liao, L.-Q. Chen, T. R. Shrout, and S. Zhang, Ultrahigh piezoelectricity in ferroelectric ceramics by design, Nat. Mater. **17**, 349 (2018).

[2] F. Li, M. J. Cabral, B. Xu, Z. Cheng, E. C. Dickey, J. M. LeBeau, J. Wang, J. Luo, S. Taylor, W. Hackenberger, L. Bellaiche, Z. Xu, L.-Q. Chen, T. R. Shrout, and S. Zhang, Giant piezoelectricity of Sm-doped $Pb(Mg_{1/3}Nb_{2/3})O_3$-$PbTiO_3$ single crystals, Science **364**, 264 (2019).

[3] W. Liu and X. Ren, Large piezoelectric effect in Pb-free ceramics, Phys. Rev. Lett. **103**, 257602 (2009).

[4] B. Narayan, J. S. Malhotra, R. Pandey, K. Yaddanapudi, P. Nukala, B. Dkhil, A. Senyshyn, and R. Ranjan, Electrostrain in excess of 1% in polycrystalline piezoelectrics, Nat. Mater. **17**, 427 (2018).

[5] S. Yang, H. Bao, C. Zhou, X. Ren, Y. Wang, Y. Matsushita, Y. Katsuya, M. Tanaka, K. Kobayashi, X. Song, and J. Gao, Large magnetostriction from morphotropic phase boundary in ferromagnets, Phys. Rev. Lett. **104**, 197201 (2010).

[6] E. Dagotto, *Nanoscale Phase Separation and Colossal Magnetoresistance* (Springer-Verlag, New York, 2003).

[7] K. Uchino, *Piezoelectric Actuators and Ultrasonic Motors* (Kluwer Academic, Boston, 1996).

[8] B. Jaffe, W. R. Cook, and H. Jaffe, *Piezoelectric Ceramics* (Academic Press, Marietta, 1971).

[9] "EU-directive 2002/95/EC": Restriction of the use of certain hazardous substances in electrical and electronic equipment (RoHS), OJEU **46**, 19 (2003).

[10] J. Wu, Perovskite lead-free piezoelectric ceramics, J. Appl. Phys. **127**, 190901 (2020).

[11] S. Supriya, A critical review on crystal structure mechanisms, microstructural and electrical performances of $Bi_{0.5}Na_{0.5}TiO_3$-$SrTiO_3$ perovskites, J. Electroceramics **49**, 94 (2022).

[12] S. Supriya, A review on lead-free-$Bi_{0.5}Na_{0.5}TiO_3$ based ceramics and films: Dielectric, piezoelectric, ferroelectric and energy storage performance, J. Inorg. Organomet. Polym. Mater. **32**, 3659 (2022).

[13] D. S. Keeble, F. Benabdallah, P. A. Thomas, M. Maglione, and J. Kreisel, Revised structural phase diagram of $(Ba_{0.7}Ca_{0.3}TiO_3)$-$(BaZr_{0.2}Ti_{0.8}O_3)$, Appl. Phys. Lett. **102**, 092903 (2013).

[14] D. Damjanovic, A. Biancoli, L. Batooli, A. Vahabzadeh, and J. Trodahl, Elastic, dielectric, and piezoelectric anomalies and Raman spectroscopy of $0.5Ba(Ti_{0.8}Zr_{0.2})O_3$-$0.5(Ba_{0.7}Ca_{0.3})TiO_3$, Appl. Phys. Lett. **100**, 192907 (2012).

[15] M. Acosta, N. Khakpash, T. Someya, N. Novak, W. Jo, H. Nagata, G. A. Rossetti, Jr., and J. Rodel, Origin of the large piezoelectric activity in $(1\text{-}x)Ba(Zr_{0.2}Ti_{0.8})O_3$-$x(Ba_{0.7}Ca_{0.3})TiO_3$ ceramics, Phys. Rev. B **91**, 104108 (2015).

[16] K. Brajesh, K. Tanwar, M. Abebe, and R. Ranjan, Relaxor ferroelectricity and electric-field-driven structural transformation in the giant lead-free piezoelectric (Ba, Ca)(Ti, Zr)O_3, Phys. Rev. B **92**, 224112 (2015).

[17] Y. Nahas, A. R. Akbarzadeh, S. Prokhorenko, S. Prosandeev, R. Water, I. Kornev, J. Íñiguez, and L. Bellaiche, Microscopic origins of the large piezoelectricity of leadfree (Ba, Ca)(Zr, Ti)O_3, Nat. Commun. **8**, 15944 (2017).

[18] Y. Saito, H. Takao, T. Tani, T. Nonoyama, K. Takatori, T. Homma, T. Nagaya, and M. Nakamura, Lead-free piezoceramics, Nature (London) **432**, 84 (2004).

[19] W. Ge, J. Li, D. Viehland, Y. Chang, and G. L. Messing, Electric-field-dependent phase volume fractions and enhanced piezoelectricity near the polymorphic phase boundary of $(K_{0.5}Na_{0.5})_{1-x}Li_xNbO_3$ textured ceramics, Phys. Rev. B **83**, 224110 (2011).

[20] M. H. Lee, D. J. Kim, J. S. Park, S. W. Kim, T. K. Song, M. H. Kim, W. J. Kim, D. Do, and I. K. Jeong, High-performance lead-free piezoceramics with high Curie temperatures, Adv. Mater. **27**, 6976 (2015).

[21] I. Levin, I. M. Reaney, E.- M. Anton, W. Jo, J. Rödel, J. Pokorny, L. A. Schmitt, H.- J. Kleebe, M. Hinterstein, and J. L. Jones, Local structure, pseudosymmetry, and phase transitions in $Na_{1/2}Bi_{1/2}TiO_3$-$K_{1/2}Bi_{1/2}TiO_3$ ceramics, Phys. Rev. B **87**, 024113 (2013).

[22] R. Garg, B. N. Rao, A. Senyshyn, P. S. R. Krishna, and R. Ranjan, Lead-free piezoelectric system $(Na_{0.5}Bi_{0.5})TiO_3$-$BaTiO_3$: Equilibrium structures and irreversible structural transformations driven by electric field and mechanical impact, Phys. Rev. B **88**, 014103 (2013).

[23] G. D. Adhikary, D. K. Khatua, A. Senyshyn, and R. Ranjan, Long-period structural modulation on the global length scale as the characteristic feature of the morphotropic phase boundaries in the $Na_{0.5}Bi_{0.5}TiO_3$-based lead-free piezoelectrics, Acta Mater. **164**, 749 (2019).

[24] C. Ma, H. Guo, and X. Tan, A new phase boundary in $(Bi_{1/2}Na_{1/2})TiO_3$-$BaTiO_3$ revealed via a novel method of electron diffraction analysis, Adv. Funct. Mater. **23**, 5261 (2013).

[25] G. D. Adhikary, D. Sharma, P. Punetha, G. Jafo, G. Abebe, A. Mishra, A. Senyshyn, and R. Ranjan, Preponderant influence of disordered *P*4*bm* phase on the piezoelectricity of critical compositions of $Na_{0.5}Bi_{0.5}TiO_3$-based ferroelectrics, Phys. Rev. B **104**, 184102 (2021).

[26] T. W. Surta, T. A. Whittle, M. A. Wright, H. J. Niu, J. Gamon, Q. D. Gibson, L. M. Daniels, W. J. Thomas, M. Zanella, P. M. Shepley, Y. Li, A. Goetzee-Barral, A. J. Bell, J. Alaria, J. B. Claridge, and M. J. Rosseinsky, One site, two cations, three environments: s^2 and s^0 electronic configurations generate Pb-free relaxor behavior in a perovskite oxide, J. Am. Chem. Soc. **143**, 1386 (2021).

[27] S.- T. Zhang, A. B. Kounga, E. Aulbach, H. Ehrenberg, and J. Rödel, Giant strain in lead-free piezoceramics $Bi_{0.5}Na_{0.5}TiO_3$-$BaTiO_3$-$K_{0.5}Na_{0.5}NbO_3$ system, Appl. Phys. Lett. **91**, 112906 (2007).

[28] G. D. Adhikary, G. J. Muleta, G. A. Tina, D. Sharma, B. Mahale, L. L. D. Silva, M. Hinterstein, A. Senyshyn, and R. Ranjan, Structural insights into electric field induced polarization and strain responses in $K_{0.5}Na_{0.5}NbO_3$ modified morphotropic phase boundary compositions of $Na_{0.5}Bi_{0.5}TiO_3$-based lead-free piezoelectrics, Phys. Rev. B **107**, 134108 (2023).

[29] X. Liu and X. Tan, Giant strains in non-textured $(Bi_{1/2}Na_{1/2})TiO_3$-based lead-free ceramics, Adv. Mater. **28**, 574 (2016).

[30] G. D. Adhikary, V. Dwij, A. Senyshyn, V. Sathe, and R. Ranjan, Large nonlinear electrostrain and piezoelectric response in nonergodic $(Na,\ K)_{0.5}Bi_{0.5}TiO_3$: Synergy of structural disorder and

tetragonal phase in proximity to a morphotropic phase boundary, Phys. Rev. Mater. **5**, 064414 (2021).

[31] F. Cordero, F. Craciun, F. Trequattrini, E. Mercadelli, and C. Galassi, Phase transitions and phase diagram of the ferroelectric perovskite $(Na_{0.5}Bi_{0.5})_{1-x}Ba_xTiO_3$ by anelastic and dielectric measurements, Phys. Rev. B **81**, 144124 (2010).

[32] Y. Hiruma, K. Yoshii, H. Nagata, and T. Takenaka, Investigation of phase transition temperatures on $(Bi_{1/2}Na_{1/2})TiO_3$-$(Bi_{1/2}K_{1/2})TiO_3$ and $(Bi_{1/2}Na_{1/2})TiO_3$-$BaTiO_3$ lead-free piezoelectric ceramics by electrical measurements, Ferroelectrics **346**, 114 (2007).

[33] G. D. Adhikary, B. Mahale, B. N. Rao, A. Senyshyn, and R. Ranjan, Depoling phenomena in $Na_{0.5}Bi_{0.5}TiO_3$-$BaTiO_3$: A structural perspective, Phys. Rev. B **103**, 184106 (2021).

[34] C. Ma, H. Guo, S. P. Beckman, and X. Tan, Creation and destruction of morphotropic phase boundaries through electrical poling: A case study of lead-free $Bi_{1/2}Na_{1/2}TiO_3$-$BaTiO_3$ piezoelectrics, Phys. Rev. Lett. **109**, 107602 (2012).

[35] J. E. Daniels, W. Jo, J. Rödel, and J. L. Jones, Electric-field-induced phase transformation at a lead-free morphotropic phase boundary: Case study in a 93%$(Bi_{0.5}Na_{0.5})TiO_3$-7%$BaTiO_3$ piezoelectric ceramic, Appl. Phys. Lett. **95**, 032904 (2009).

[36] M. Hinterstein, L. Schmitt, M. Hoelzel, W. Jo, J. Rödel, H.-J. Kleebe, and M. Hoffman, Cyclic electric field response of morphotropic $Bi_{1/2}Na_{1/2}TiO_3$-$BaTiO_3$ piezoceramics, Appl. Phys. Lett. **106**, 222904 (2015).

[37] W. Jo, J. E. Daniels, J. L. Jones, X. Tan, P. A. Thomas, D. Damjanovic, and J. Rödel, Evolving morphotropic phase boundary in lead-free $Bi_{1/2}Na_{1/2}TiO_3$-$BaTiO_3$ piezoceramics, J. Appl. Phys. **109**, 014110 (2011).

[38] See Supplemental Material at http://link.aps.org/supplemental/10.1103/PhysRevB.108.224105 for (i) specimen preparation and characterization, (ii) polarization versus electric field for different compositions, and (iii) in situ XRD measurements with unipolar electric field data.

[39] B. N. Rao and R. Ranjan, Electric-field-driven monoclinic-to-rhombohedral transformation in $Na_{0.5}Bi_{0.5}TiO_3$, Phys. Rev. B **86**, 134103 (2012).

[40] R. Ranjan and A. Dviwedi, Structure and dielectric properties of $(Na_{0.50}Bi_{0.50})_{1-x}Ba_xTiO_3$: $0 \leqslant x \leqslant 0.10$, Solid State Commun. **135**, 394 (2005).

[41] C. Ma and X. Tan, Phase diagram of unpoled lead-free $(1-x)(Bi_{1/2}Na_{1/2})TiO_3$-$xBaTiO_3$ ceramics, Solid State Commun. **150**, 1497 (2010).

[42] C. Ma, X. Tan, E. Dul'kin, and M. Roth, Domain structure-dielectric property relationship in lead-free $(1-x)(Bi_{1/2}Na_{1/2})TiO_3$-$xBaTiO_3$ ceramics, J. Appl. Phys. **108**, 104105 (2010).

[43] C. Ma and X. Tan, In situ transmission electron microscopy study on the phase transitions in lead-free $(1-x)(Bi_{1/2}Na_{1/2})TiO_3$-$xBaTiO_3$ ceramics, J. Am. Ceram. Soc. **94**, 4040 (2011).